Interlayer charge transfer in graphene–2D polyimide heterostructures

2D Materials

PAPER

Interlayer charge transfer in graphene–2D polyimide heterostructures

Francesca Falorsi[1,11], Shuangjie Zhao[2,11], Kejun Liu[2,3], Christian Eckel[1], Jonas F Pöhls[1], Wiebke Bennecke[1], Marcel Reutzel[1], Stefan Mathias[1,4], Kenji Watanabe[5], Takashi Taniguchi[6], Zhiyong Wang[2,7], Miroslav Polozij[2,8,9], Xinliang Feng[2,7], Thomas Heine[2,8,9,10] and R Thomas Weitz[1,4,*]

[1] Georg-August-University of Göttingen, Friedrich-Hund-Platz 1, 37077 Göttingen, Germany
[2] Faculty of chemistry and food chemistry, Technical University of Dresden, Bergstrasse 66, 01069 Dresden, Germany
[3] Functional Nano & Soft Materials (FUNSOM), Jiangsu Key Laboratory for Carbon-Based Functional Materials & Devices, Soochow University, 215123 Suzhou, People's Republic of China
[4] Göttingen ICASEC, 37077 Göttingen, Germany
[5] Research Center for Electronic and Optical Materials, National Institute for Materials Science, 1-1 Namiki, Tsukuba 305-0044, Japan
[6] Research Center for Materials Nanoarchitectonics, National Institute for Materials Science, 1-1 Namiki, Tsukuba 305-0044, Japan
[7] Max Planck Institute of Microstructure Physics, 06120 Halle (Saale), Germany
[8] Helmholtz-Zentrum Dresden-Rossendorf, HZDR, Bautzner Landstr. 400, 01328 Dresden, Germany
[9] Center for Advanced Systems Understanding, CASUS, Untermarkt 20, 02826 Görlitz, Germany
[10] Department of Chemistry, Yonsei University, Seodaemun-gu, Seoul 120-749, Republic of Korea
[11] These authors contributed equally.
[*] Author to whom any correspondence should be addressed.

E-mail: thomas.weitz@uni-goettingen.de

Keywords: 2D covalent organic framework, graphene, heterostructure, SNOM, Raman, electronic properties

Supplementary material for this article is available online

OPEN ACCESS

RECEIVED
29 August 2024

REVISED
13 December 2024

ACCEPTED FOR PUBLICATION
21 January 2025

PUBLISHED
4 February 2025

Abstract

The vertical integration of multiple two-dimensional (2D) materials in heterostructures, held together by van der Waals forces, has opened unprecedented possibilities for modifying the (opto-)electronic properties of nanodevices. This not only allows for the exploration of new physical phenomena but also greatly broadens the application horizon of existing monolayer devices. Graphene, with its remarkable opto-electronic properties, is an ideal candidate for such applications. The other potential candidates are 2D polymers, crystalline polymeric materials with customizable structures and electronic properties, as they can be synthesized in all mathematically possible Bravais lattices. In this study, we investigated the optoelectronic properties of a heterostructure created by pristine graphene and a rectangular 2D polyimide (2DPI) film. This imprints a new superlattice on graphene in conjunction with a direct influence on its electronic properties. Theoretical and experimental analyses reveal that interlayer charge exchange between the 2D polymer and graphene induces hole doping in the graphene layer. We have also observed that the properties of the heterostructure are dependent on the substrate used in experiments, likely due to the porous character of the 2DPI allowing direct interaction of graphene with the support. Furthermore, we demonstrate a direct correlation between the thickness of the 2DPI layer and the extent of hole doping in graphene. These findings highlight the unique ability to tailor functionalities in 2D polymers-based heterostructures, opening avenues for the development of optoelectronic devices with precisely engineered properties and stimulating further exploration of the diverse phenomena accessible through tailored designs of the 2D polymers.

In the past decades, the rise of graphene [1, 2] and other two-dimensional (2D) materials has offered an unprecedented possibility to combine them to layer-stacked heterostructures (HS) held together by van der Waals (vdW) forces. Strong interlayer effects enable access to new and interesting physical phenomena [3]. Prominent examples include the band gap opening in bilayer graphene

[4], the indirect-to-direct band gap transition in transition metal dichalcogenides [5–7], and the semiconductor-to-metal transition in noble metal dichalcogenides [8, 9]. However, graphene and other 2D crystals have fixed lattice structures that are limited in their tunability and modification. To increase structural flexibility and enable functional designs, 2D polymers and their layer-stacked variant, 2D covalent organic frameworks (COFs), have been developed for HS in recent years [10–15]. 2D polymers are crystalline, layered materials with organic building blocks connected laterally via covalent bonds with monolayer or few-layer (<10) thickness. Notably, 2D polymers can form all mathematically possible 2D lattices (e.g. hexagonal, square, kagome) [16, 17], directly influencing their electronic band structure, which can be metallic, semiconducting, or exhibit topological bands, Dirac points, and flat bands. Additionally, their chemical composition is highly modifiable, affecting the work function and interlayer charge exchange, thereby altering the density of states (DoS). Having these novel materials with tunable intriguing properties, it is expected that when coupled with graphene, novel physical phenomena can be induced into graphene.

In this work, we investigate the electrical and spectroscopic properties of a HS of monolayer graphene with a 2D rectangular polyimide (figure 1(a)) (denoted below as 2DPI/graphene). The ultrafast interlayer charge transfer between this 2D polyimide (2DPI) and chemically exfoliated graphene has already been shown by some of us [13]. Here, we further investigate these HSs by combining high-quality exfoliated graphene with 2DPI film of different thicknesses. This approach allows us to analyze both the interlayer charge transfer in the HS as well as the impact of the 2DPI on the charge transport within the graphene layer. As we detail below, the 2D polymer induces hole doping in the graphene, and the strength of the doping increases with the layer number of the polymer. In our analysis we have utilized a large number of complementary methods, not only to give a full characterization of the HSs but also to give reference data for future HSs of the similar type.

We first extensively utilize theoretical models to explain the electronic properties of the 2DPI/graphene HS. Standard theoretical models of layered materials, which only consider standalone layers in vacuum, are not suitable for the 2D polymer/graphene system. This stems from the porous nature of the 2DPI with pores large enough for the graphene to interact through the 2DPI layer with the substrate under it. To take this effect into account, we have investigated three different models; (i) standalone 2DPI/ graphene, (ii) 2DPI/graphene deposited on SiO_2 as in transport experiments, using 2D SiO_2 [18] as a substrate model, denoted SiO_2/2DPI/graphene, (iii) 2DPI/graphene deposited on Si as in angle-resolved photoemission spectroscopy (ARPES) experiments, using a H-terminated 4-layer 2D model of Si(100) surface as a substrate model, denoted Si/2DPI/graphene (figure 1(b)).

There are two important structural effects influencing the graphene in the HS with the porous 2D polymer. Due to the vdW interaction between the 2DPI and graphene, a superlattice forms in graphene mirroring the lattice structure of the polyimide. This is manifested by the corrugation of graphene towards the 2DPI pore. In the case of standalone 2DPI/graphene HS, the corrugation amplitude is about 1.12 Å, however, with Si and SiO_2 substrates, the maximum deformation of graphene towards the support is 1.5 Å and the total corrugation amplitude is almost 3 Å (figure 1(c)). The second structural effect on graphene comes from the relative rotation of the graphene and 2DPI layers. Experimentally, such an angle is very hard to control due to the polycrystalline nature of the 2DPI used and should be considered random. This causes the superlattice imposed on graphene to be in different orientations with respect to the graphene lattice. To investigate this, we have tested several rotation angles (0°, 4°, 12.6° and, 21.6°), which produce models with small enough unit cells to study their electronic properties.

In the case of the standalone 2DPI/graphene, the HS band structure is a simple superposition of the 2DPI and graphene band structures, irrespective of the rotation angle (figures S1 and S2)). More pronounced electronic changes can be seen with the introduction of a substrate (SiO_2 or Si). Due to the size of the systems, we were not able to include the substrate directly in most electronic properties calculations. Instead, we only used it to obtain the HS geometry and removed the substrate for the band structure calculation. This does not bring any significant error; see the example of Si/2DPI/graphene in figure S3. The introduction of a SiO_2 substrate does not bring any changes to the 2DPI/graphene band structure (figure S4). On the other hand, with the introduction of a Si substrate, a gap of 7.5 meV opens at the Dirac cone, independent of the HS rotational angle (figures 1(d), S6). A more significant change is seen in the DoS (figures 1(e), S4 and S5) for both the SiO_2 and Si supported HS, where two distinct peaks emerge below and above the Fermi level, instead of a single peak above the Fermi level in the standalone HS. This relates to the difference in charge transfer between the 2DPI and graphene (figures 1(f), S12), which is much stronger in the corrugated structures of the substrate-deposited HS.

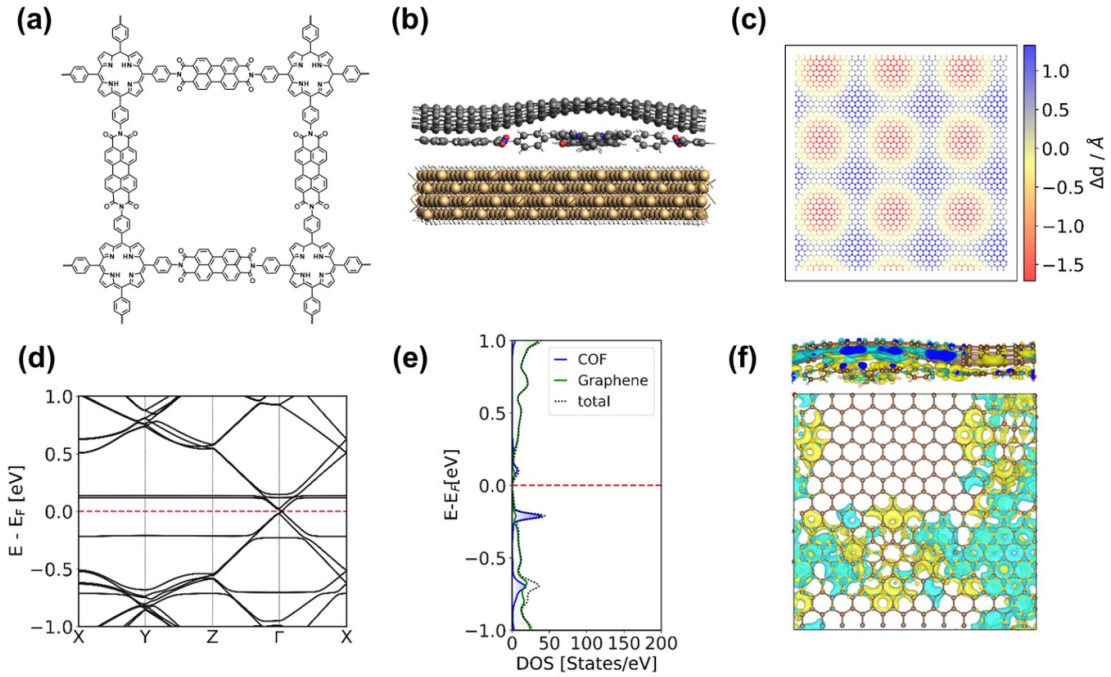

Figure 1. (a) Chemical structure of studied 2DPI. (b) Atomic structure of Si/2DPI/graphene (c) Corrugation of graphene induced by 2D-polymer and substrate Si/2DPI/graphene (red: graphene bent towards polymer, blue: graphene bent from polymer), forming square superlattice. (d) Band structure of 2DPI/graphene moiety of Si/2DPI/graphene structure. (e) Projected density of states of 2DPI/graphene moiety of Si/2DPI/graphene structure. (f) Visualization of charge distribution difference 2DPI/graphene moiety Si/2DPI/graphene. (Yellow: charge accumulation. Light blue: charge depletion).

1. Electronic properties of 2DPI/graphene HS

To experimentally analyze the optoelectronic properties of the 2DPI/graphene HS, we first focus on the SiO_2 supported system. This brings the additional advantage that the SiO_2 is insulating and can be used as dielectric in a field-effect transistor geometry allowing to electrostatically tune the Fermi level in the HS. The optoelectronic properties of the HSs were then analyzed with three complementary measurements: electrical measurements, scattering-type scanning near-field optical microscopy (SNOM) and Raman spectroscopy. Multiple samples were studied, where exfoliated graphene flakes were deposited onto 2DPI films via a dry transfer method (described in [19]). An overview of all the samples and the techniques used for their experimental analysis is presented in S7. The monolayer 2DPI was synthesized as described by our previous report [12] using the Langmuir–Blodgett method and has a homogeneous thickness of 0.8 nm [13]. To facilitate the comparison between the HS configuration and bare graphene, a portion of the graphene had been stamped onto SiO_2 so that the optical properties of bare graphene and the HS can be compared.

A typical image of a SiO_2/2DPI/graphene HS is shown in figure 2(a). Here, the HS is mapped using SNOM, where in addition to the topographic information we can record local differences in optical conductivity. The near-field optical signal is indeed directly linked to the amplitude and phase of the electromagnetic field inside the nanogap between the tip and the sample and is thus related to the complex optical conductivity of the sample [20]. Thus, the optical contrast difference between HS and bare graphene can be attributed to a difference in doping and mobility between them. Figure 2(a) shows the 3rd harmonic optical amplitude taken with a laser excitation energy of around 115 meV normalized to the gold signal. The optical amplitude in graphene is larger compared to the HS region. In this sample, we have also studied the excitation-energy dependent relative contrast between 115 meV and 134 meV, where the contrast between the HS and the bare graphene diminishes with increasing excitation energy. Figure 2(b) summarizes this trend where the difference in contrast of the gold normalized 3rd harmonic optical amplitude of the HS and the graphene is shown as a function of excitation energy. At lower excitation energies, where Drude intraband conductivity dominates the optical response, the reduced optical amplitude of the HS compared to the graphene region can be attributed to increased electron scattering, likely caused by defects introduced by the 2DPI. This suggests lower electron mobility in the HS. Additionally, differences in doping between the two regions could also contribute to the variation in optical contrast. If the bare graphene region has a lower Fermi energy, its optical response may result from a combination of Drude intraband transitions and interband transitions [21,

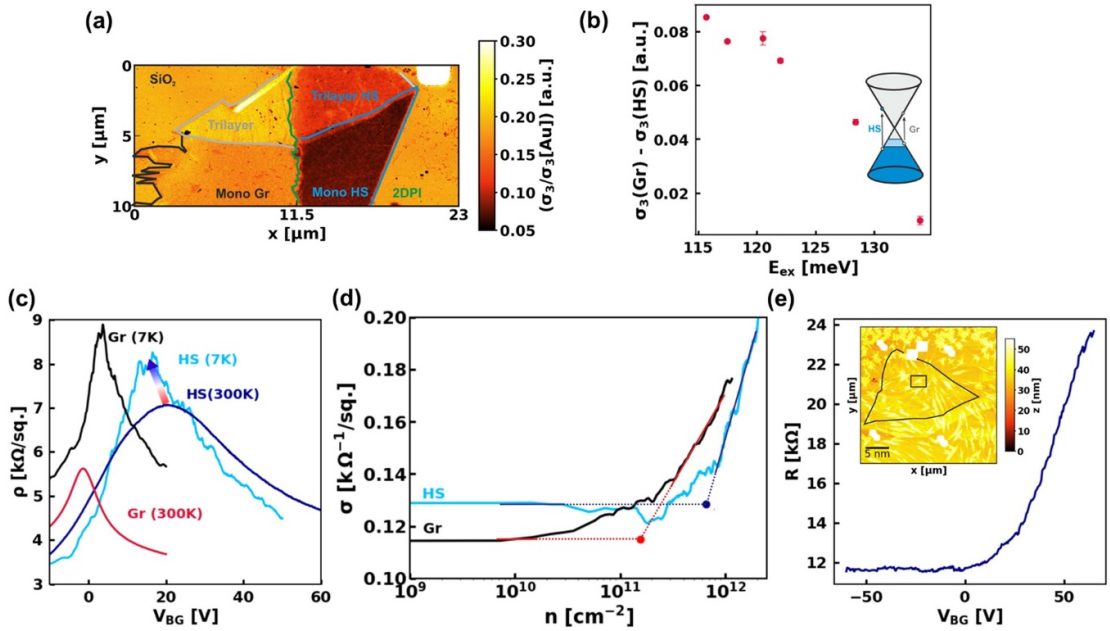

Figure 2. (a) 3rd harmonic near field optical amplitude at 115 meV of one of the samples studied. In the upper part of the flake, a trilayer graphene is present, as highlighted by the colored lines. In this sample, part of the exfoliated graphene has been transferred to the 2DPI monolayer on the SiO_2 to allow the comparison. A significant decrease in the σ_3 in the HS is observed due to a change in the optical conductivity between the HS and the graphene. (b) Energy dependent difference between the normalized 3rd harmonic optical signal of the graphene and the HS part of the samples shown in (a). In the insets, the process associated with the higher excitation energies is shown: both the graphene and the HS are dominated by the interband process. (c) Gate sweep measurement over the Si^+ back gate sample prepared on a SiO_2/Si^+ wafer. In this sample part of the flake is stamped on the SiO_2 while part on the monolayer 2DPI. The measurement is performed under a vacuum. The HS shows hole doping compared to the bare graphene part of the sample. Low-temperature measurements show that the HS maintains the Dirac peak behavior until 7 K. (d) The residual charge carrier density estimates, obtained from the low-temperature sweeps of the graphene and HS curves shown in (c), and determined by the intersection between the horizontal and the linear fits of the conductivity plotted as a function of n in logarithmic scale. The values obtained are $\delta n_{Gr} = 0.16 \times 10^{11}$ cm^{-2} for graphene and $\delta n_{HS} = 0.66 \times 10^{11}$ cm^{-2} for the HS, indicating higher disorder in the HS. (e) Gate sweep measurements, (over the Si^+ gate) performed under vacuum at 7 K over the HS shown in the inset with an AFM picture. In the inset, the thick black line shows the borders of the graphene flake and the black rectangle highlights the single 20 nm crystal contacted for this measurement, as described in the method section. The Dirac peak is not visible until an application of 60 V over the back gate. Similar behavior where shown by the other crystals in the flake, for none of which the Dirac peak could be visualized. The thicknesses of the crystals are ranging from 7 to 20 nm.

22]. At high excitation energies, intraband transitions dominate the optical response, as indicated by the inset in figure 2(b), making it independent of both doping and mobility. As a result, the graphene and the HS exhibit the same optical contrast [23–26]. Finally, we note that the SNOM images of the HS appear very homogeneous, which implies that at the scale of the resolution (around 50 nm) the doping is uniform.

The optical SNOM images demonstrate the impact of 2DPI on the optical conductivity of graphene, attributed to a combination of doping and mobility changes in the HSs. To further understand the effects of 2DPI on graphene's transport properties, we conducted direct electrical transport measurements on various samples. In figure 2(c) a gate sweep of the HS shown in figure S9a is presented and compared to a gate sweep of the same graphene flake which is not in contact with the 2DPI. From the relative position of the charge neutrality point of the two devices, we are able to identify the relative doping level. The 2DPI induces hole doping in the graphene; in this case of $\Delta n = (1.55 \pm 0.01) \times 10^{12}$ cm^{-2}. The calculations are performed as described in the electrical measurement paragraph of the Methods section. The 2DPI also induces additional scattering [27] as we can identify by a decrease of the charge carrier mobility from 1580 to 901 cm^2 Vs^{-1} (at 1×10^{12} cm^{-2}) and by an increase of the width of the charge neutrality peak [28]. Finally, by performing temperature-dependent measurements, we could verify that the Dirac peak behavior of graphene is maintained up to 7 K, as expected by the DFT calculations shown in figure 1(d). At low temperatures the defects in graphene are less screened by thermal fluctuation, thus an increase in the resistance oscillations is seen both in the bare graphene and HS part. The greater oscillations in the HS are attributed to the presence of a larger number of defects and traps induced in the graphene by the 2DPI [28]. The higher disorder caused by these defects in the HS is also evident by the fact that the resistivity at the CNP shows a smaller increase in the HS compared to the bare graphene region at low temperatures (represented by the black and light blue plots in figure 2(c),

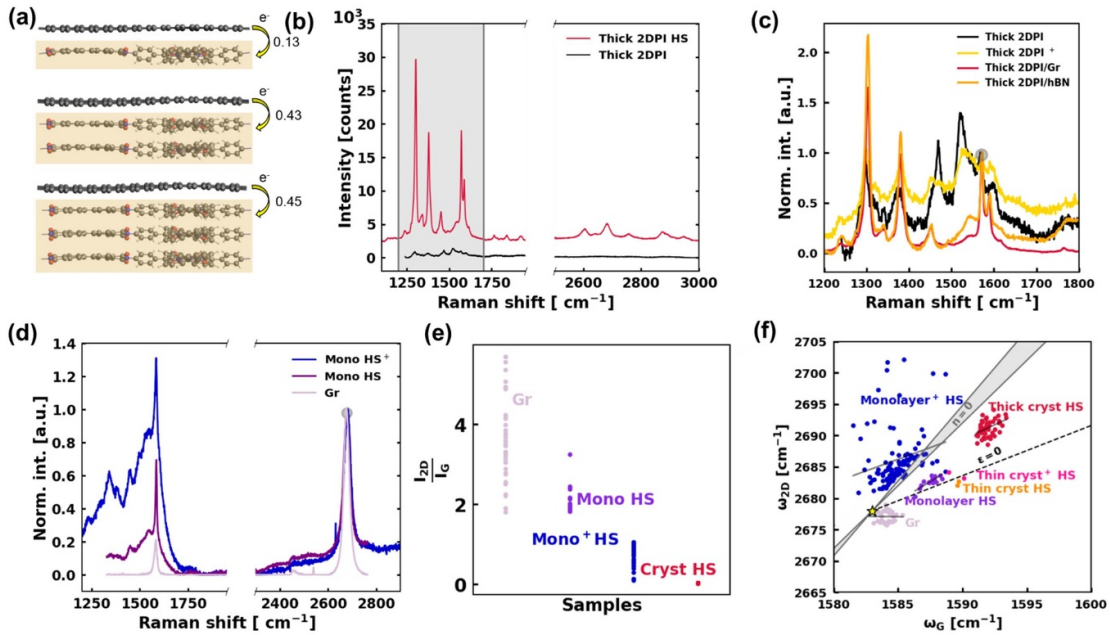

Figure 3. (a) Representation of graphene HS with one, two or, three layers of 2D polyimide and net electron transfer per unit cell. (b) Comparison of the Raman spectra taken on a sample with thick crystals: in black the spectrum of the untreated crystals, and in red the one of the thick 2DPI/graphene HS. To both spectra the background has been subtracted and, to the graphene one, an offset of 2500 has been added for better visualization. The range indicated in the shaded gray region is shown in figure (c) where the shown spectra are normalized with respect to the peak at $\omega \sim 1570$ cm^{-1}, circled in the figure, and prominent in each spectrum. Here there are two additional spectra than in (a): in yellow is shown the spectrum of the protonated crystals and in orange the spectrum of the 2DPI/hBN stack sample. (d) Comparison of the Raman spectra taken 2 samples in which the graphene is placed on top of a 2D polyimide monolayer. The pink and purple spectra are taken from the same sample respectively on the HS and the bare graphene part. The spectrum in blue belongs to a sample in which the monolayer 2DPI has been protonated before the graphene transfer. (e) Ratio between the intensity of the 2D peak and the G peak of different graphene samples. Since the ratio decreases both with the protonation and the presence of the thicker 2DPI, confirms the hypothesis that the charge transfer between the two materials increases with the increasing number of polyimide layers underneath and with the protonation of 2DPI upon stamping. (f) Raman spectra analysis comparing different samples. Here the ω_G is plotted in respect of ω_{2D} all the different types of samples studied. The spots mainly lay parallel to the line corresponding to null strain ($\varepsilon = 0$), showing that the doping has a stronger effect than the strain on the graphene. The shift of the ω_G to higher values with thicker samples supports the hypothesis that the doping increases with increases in 2DPI thickness.

respectively). The residual charge carrier density induced by the disorder around the CNP can be calculated from the intersection between the horizontal and linear fits of the conductivity plotted against the logarithmic charge carrier density, as shown in figure 2(d) [29, 30]. This analysis yields a higher value of the residual charge carrier density in the HS part of the flake, respectively of $\delta n_{Gr} = 1.6 \times 10^{11}$ cm^{-2} for graphene and $\delta n_{HS} = 6.6 \times 10^{11}$ cm^{-2} for the HS.

Having established the 2DPI/graphene HS, we also have used the versatility of the chemical synthesis method to realize 2DPI films with varying thicknesses and transfer graphene onto them. In general, increasing the layer number of the 2DPI should increase the intralayer charge transfer due to an increased work function in the 2DPI as a function of layer thickness, as was seen in other 2D materials [31–34]. In fact, we do observe this in our transport measurements of graphene stamped on thicker 2DPI crystals, an example of which is shown in figures 2(e), S10(b) where in our accessible back gate window we are not able to electrostatically dope the graphene in the HS to the charge neutrality point, indicative of a doping density larger than $\sim 4.6 \times 10^{12}$ cm^{-2}. These findings are consistent with our first-principle calculations. As shown in figure 3(a), adding more layers of the 2DPI leads to a substantial increase in charge transfer to graphene. It also leads to a significant downshift of the Fermi level, which can be attributed to the p-doping of graphene (figure S11). Our calculations show that the 2DPI has a higher work function than graphene; 4.56 eV versus 4.45 eV, which is consistent with the acceptor-character of the porphyrin sites [27, 35, 36], which also show a larger charge transfer as shown in figures 1(e) and S12. These doping effects cannot be verified solely through transport measurements, as an accurate estimation of doping requires visualization of the Dirac peak. Therefore, an alternative method should be employed for comparing samples of different thicknesses, as described in the following.

2. Spectroscopic analysis of doping and strain

To compare the interaction effects across different types of samples and to obtain large sample statistics, we used Raman spectroscopy, which also allows

for the distinction between doping and strain effects in the different HS samples. Strain is predicted to be present in the HS (figure 1(c)) along with doping.

Typical Raman spectra of various 2DPI and 2DPI/graphene HSs are shown in figures 3(b)–(d) (please note that in figures 3(b) and (c) we have used 2DPI multilayers and in figures 3(d) a 2DPI monolayer for the HS). One of the most striking effects is the enhancement of the peak intensities in the multilayer 2DPI/graphene HS compared to the bare 2DPI. In general, two main mechanisms are known that can lead to Raman enhancement in thin multilayers of this type, namely chemical enhancement and optical interference. The mechanism referred to as chemical enhancement includes various factors, such as charge transfer and orbital coupling [37–39]. Optical interference involves constructive interference of multiple reflections of the excitation light beam through the various layers of the sample [40, 41], and therefore is known as interference-enhanced Raman scattering, and depends critically on the dielectric constant of the layers involved. For an initial understanding of which mechanism underlies the Raman enhancement, we have investigated different types of samples: pure 2DPI, 2DPI which was protonated to mimic doping without the presence of additional layers, 2DPI/graphene and, 2DPI/hBN, as shown in figures 3 and S13. Additionally, we tested different thicknesses of the 2DPI film.

To start the disentanglement between the effects stemming from the dielectric environment and charge transfer we placed a thin hBN flake (around 5 nm thick) and a graphene flake next to one another on the same thick 2DPI film. In both cases (in the 2DPI/graphene and 2DPI/hBN HSs) the Raman signal is enhanced by more than one order of magnitude, with distinct enhancement factors for different peaks. For instance, the enhancement factors for the peak at $\omega_1 = 1301$ cm^{-1} are 21 and 32 for hBN and graphene HS respectively. One aspect contributing to the enhancement could be interference effects. Specifically at the 532 nm excitation energy used in this experiment, the conditions to obtain an interference enhanced Raman scattered signal are met. In contrast, while with an excitation energy of 633 nm the 2DPI peaks are still enhanced in the 2DPI/graphene HS, they are not enhanced in the 2DPI/hBN HSs. We attribute this difference of enhancement to the dissimilar dielectric constant of hBN and graphene in the visible wavelength, with the consequence that no interference enhancement is taking place for the hBN HS (see figures (S13), (f)). A second aspect is that the chemical enhancement, induced by the charge transfer between the 2DPI and the graphene, will also contribute to enhancing the Raman signal. A method to validate the impact of chemical enhancement on the Raman signal is to purposely dope (protonate) the pure 2DPI with hydrochloric acid. Indeed, protonation leads to an enhancement of the same Raman peaks (figures (S13), (c)) as in the 2DPI/graphene HS. For instance, the peak at $\omega_2 = 1381$ cm^{-1} is enhanced by a factor of 2. The normalized spectra presented in figure 3(c) show that the relative intensity of different peaks undergoes similar changes in the doped 2DPI and also in the two HSs investigated.

We can further validate the relative roles of chemical and interference enhancement by investigating monolayer 2DPI HSs. The study of the HSs created with monolayer 2DPI (figures 3(d) and S13(b)) indicates that chemical enhancement continues to play a role, while interference enhancement does not contribute significantly. We conclude this from a study performed with h-BN of different thicknesses on top of a 2DPI (figure S13), where no enhancement can be observed. This lack of interference enhancement, combined with a smaller charge exchange in the monolayer case, results in significantly smaller enhancement in monolayer 2DPI/graphene HS compared to the thicker samples. Nevertheless, when the 2DPI is protonated prior to HS formation, the peaks are further enhanced compared to the undoped 2DPI/graphene HS (figure 3(d)) since the charge transfer between the protonated 2DPI and the graphene increases in the doped HS. For a complete picture of the effects contributing to the Raman spectra more measurements should be taken, with more excitation wavelength and varying for example the thickness of the SiO_2.

This hierarchy of charge transfer (largest charge transfer in doped thick 2DPI/graphene HSs, smallest charge transfer undoped monolayer 2DPI/graphene HSs) can be further confirmed by the analysis of the relative intensity of graphene's main spectral features, the G peak ($\omega_G \sim 1580$ cm^{-1}) and the 2D peak ($\omega_{2D} \sim 2680$ cm^{-1}) [42, 43]. The value of I(2D)/I(G) is known to be about 4 for undoped graphene and to continuously decrease as the doping of the sample increases [44]. In our experiments, the relative intensity I(2D)/I(G) was calculated in multiple spots of differently prepared devices, as shown in figure 3(e). Here it is evident that the mean I(2D)/I(G) ratio of the bare graphene decreases in the undoped monolayer 2DPI/graphene HS, and it further decreases in the protonated monolayer-2DPI HS, reaching the lowest values when the HS is formed by thick crystals. The analysis of the spectral shape of the individual 2D and G peaks allows disentangling effects from doping and strain induced into graphene by the 2DPI. It is well-known that the Raman spectrum of graphene is highly sensitive to the mechanical strain and doping level of the flakes, as strain and doping both

have a strong influence on the bond lengths and the electron-phonon coupling and directly impact the shape and the position of these two peaks. To test for the different contributions of strain and doping, the position of the 2D peak frequency ω_{2D} is plotted with respect to the G peak ω_G for multiple spots of differently prepared HSs in figure 3(f). By evaluating the slope of the experimental points with respect to the case of the unstrained and undoped graphene (ω_{G0} and ω_{2D0} indicated by the star), we disentangle the effects of the strain and doping [45, 46]. The two gray lines in figure 3(e) separate the ω_G—ω_{2D} plane in different regions. The gray area indicated with $n = 0$, with a slope $(\Delta\omega_{2D}/\Delta\omega_G)$ =2.2 ± 0.2, represents the area for which the only effect induced on the graphene is strain. Starting from $(\omega_{G0}, \omega_{2D0})$, the values moving along the dotted line indicated with $\varepsilon = 0$, characterized by a slope of $(\Delta\omega_{2D}/\Delta\omega_G) = 0.8$, define a region in which the only effect induced on the graphene by the substrate is hole doping. By projecting the experimental values on the (ω_G, ω_{2D}) onto the two characteristic $n = 0$ and $\varepsilon = 0$ lines, it is possible to deduce the strain and doping of the studied sample: the further the projected point is from the unstrained and undoped value $(\omega_{G0}, \omega_{2D0})$ the higher the sample is doped/strained. By performing a linear fit on the experimental data, shown by faint gray lines in figure 3(f), we obtained values of the slope of: S_{Gr}=−0.03 ± 0.26, S_{Mono} = 1.24 ± 0.24, $S_{Thick\ cryst}$ = 0.94 ± 0.28, S_{Mono+} = 0.75 ± 0.21. We therefore conclude that in all samples doping plays the main role since the 2D peaks of the HSs are located mostly parallel to the $\varepsilon = 0$ line. The doping density (as deduced from the G-peak position) increases according to the doping hierarchy discussed above. Finally, while some strain seems to be present in the monolayer 2DPI/graphene samples, it overall plays a minor role compared to the doping.

3. Direct analysis of graphene band structure in 2DPI/graphene HS by ARPES

Up to now, the analysis has indicated that the 2DPI induces interlayer charge transfer, charge scattering and, strain in the HS, but we have not been able to experimentally identify the expected change in the DoS in the HS. To test for these effects, we have manufactured HSs directly on conductive substrates (doped Si) to allow direct band structure measurements by ARPES (technique described in [47, 48]). In the momentum cut of the detected spectra, shown in Figure S14b, it is possible to identify that there is a dip in the acquired spectral weight at the Dirac peak. This spectral weight dip of about 215 meV, measured consistently in a second sample, can be attributed to the interaction between 2DPI and graphene, which induces a dip in the DoS in the HS, as calculated for the substrate-supported HS dip in the DoS in the HS (figure 1(d), where two distinct density peaks emerge below and above the Fermi level). The dip in the ARPES spectral weight and in the calculated thus indicates a strong interaction between graphene and 2DPI, more details of the analysis are shown in figure S14 in the SI. There, we also discuss that interaction between 2DPI and graphene when placed on a Si substrate is stronger than when SiO_2 substrates are used, as confirmed by our Raman analysis and theoretical calculations (figure S6(b)).

4. Towards larger device sizes: 2DPI/CVD graphene HS

In the measurements up to now exfoliated graphene has been used, which is ideal for fundamental studies. However, in such devices, the HS size is limited by the size of graphene to the μm regime. Since the 2DPI monolayers can be also synthesized on larger scales, we have tested HS composed of chemical vapor deposition (CVD) graphene and the 2DPI (figure (S15)). In these samples similar inter-layer charge transfer between the 2DPI and the graphene was measured, whereas the overall charge carrier mobility was lower, as expected for CVD graphene.

5. Conclusion

In conclusion, we conducted an in-depth study of the interaction between a 2D COF and graphene, using various experimental techniques and density functional theory calculations. Through electronic, scanning near-field optical microscopy and Raman spectroscopy measurements we showed that graphene is hole doped by the 2DPI. This charge transfer process is likely attributed to the work function difference between the 2DPI and graphene. Our investigation of different samples revealed that controlling the charge transfer between the polymer and graphene can be finetuned by adjusting the thickness of the 2DPI and/or protonating the 2DPI. Specifically, as the 2DPI thickens, the hole doping effect on graphene increases. The remarkable tunability observed in the interaction between this 2DPI and graphene suggests a promising avenue for further exploration. With diverse 2D polymers characterized by distinct chemical and topological properties, we anticipate the investigation of new and intriguing physical phenomena in this emerging field of study.

6. Experimental methods

6.1. Device fabrication

The stamped samples were fabricated by transferring the graphene flakes on the 2DPI substrate using the dry transfer method described in [19]. The graphene flakes were obtained through mechanical exfoliation from natural graphite crystals (from NGS trading and consulting) Silicon/Silicon dioxide (300 nm) substrate. The electrical contacts were patterned using

electron beam lithography (from Raith), with the following parameters: an accelerating voltage of 10 kV, a dose of 110 μC cm^{-2} for the 7.5 μm aperture (used for small contacts) and a dose 170 μC cm^{-2} for 60 μm (used for wider contact lines). The layer of resist for the e-beam procedure was obtained following the procedure described in [49]. Finally, the 1 nm chromium (with a rate of around 0.43 Å s^{-1}) and 60 nm gold (with a rate of around 0.9 Å s^{-1}) contacts are evaporated via thermal evaporation (evaporation chamber from BesTec) at pressures of around 10^{-6} mbar. The top electrolyte gate for the measurements, shown in figure 2, was deposited through the technique described in [50]. To separate the CVD graphene and the thick crystals samples from the surroundings, the flakes were etched through a dry etching process performed with a flow of 40 sccm O_2 plasma at 80 W and 40 mTorr for 18 s in a reactive ion etching chamber (from Oxford PlasmaLab). The etching masks were designed using electron beam lithography. In the protonated sample the protonation was performed by depositing a droplet of 10% of Hydrochloridric acid and letting it dry at 80° overnight (around 12 h).

Before preparing the samples, the stability of the studied 2DPI to the applied chemicals was assessed through the analysis of atomic force microscopy (AFM) pictures and Raman spectra; no difference was found before and after the application of any of the used chemicals.

6.2. Scanning probe techniques

The AFM measurements were performed with Asylum Jupiter AFM by Oxford Instruments with Tap300Al-G (from NanonAndMore) tips.

The near field scattering microscopy images are taken with a commercial s-SNOM (from Neaspec Company) coupled to a tunable CO_2 laser (from Access laser, model L4G) with wavelengths of 9.2–10.78 μm. The infrared nanoimaging was based on an AFM operated in tapping mode with a tapping amplitude of $\Delta z = 90$ nm. All the images were taken with the tips Arrow-NCPt (from Nanoworld) characterized by a tapping frequency Ω of $\sim$270 KHz. The power of the laser during the measurement was set to around 0.8 mW.

6.3. Raman measurements

The Raman measurements shown in the manuscript were taken with the commercially available setup is the commercially available LabRam HR Evolution (from Horiba). This setup is coupled two 2 lasers: an HeNe laser with a 6329 nm and YAG-Laser (Neodymium-doped Yttrium Aluminum Garnet) with a wavelength of 532 nm (torus 532 from Laser Quantum). The setup is equipped with 2 different gratings of 1800 gr mm^{-1} and 600 gr mm^{-1}, both were used during this work. The images shown in figure 4 are taken with the 600 gr mm^{-1} grating.

6.4. Electrical measurements

Electrical measurements, both at room temperature and low temperature, were performed by contacting the gate and the source-drain of the samples through the application of voltages to needles connected to a Keithley 2450. In measurements involving the electrolyte gate, the needles were applied directly to the droplet of electrolyte on top of the sample. The measurements under vacuum were conducted in a Lakeshore CRX-VF probe station under vacuum conditions (temperature range 5–450 K). The samples were fixed to the sample holder using silver conducting paint to ensure thermal connection between the holder and the sample.

From gate sweep measurements shown in figure 2(c), considering the field effect transistor geometry of the samples it is possible to derive the charge carrier density n induced capacitively by the Si gate, with:

$$n = \frac{\varepsilon_0 \varepsilon}{ed} (V_{BG} - V_0)$$

where d is the thickness of the SiO_2 (300 nm), is the dielectric constant of the dioxide, is the vacuum permittivity, e is the elementary electron charge, V_{BG} is the applied voltage to the back-gate and V_0 is the voltage corresponding to the CNP of the considered sample [51]. The mobility, corresponding to a defined n, was calculated from the 2 point-probe resistivity ρ from: $\mu = 1/(\rho n e)$.

6.5. Quantum chemistry calculations details

All structures are generated by hetbuilder [52] by rotating and expanding unit cells of target 2D-polymer and graphene w/wo substrate to look for the shared coincident supercell. The geometries of all multi-layer structures were optimized by density functional based tight binding method [53, 54] (DFTB), which is a computationally efficient tight binding approach based on density functional theory. DFTB+ [55], as an implementation of DFTB, was used to perform the geometry optimizations by matsci–0–3 parameters [56]. Electronic properties like band structures and DoS were performed by Fritz-Haber-Institute *ab-initio* materials simulations package (FHI-aims [57]) with PBE [58] functional plus many-body dispersion [59]. Tier 2 basis set and tight integration mesh were used. Charge transfer calculations were performed using Vienna *Ab initio* Simulation Package [60–62] with PBE functional plus D3BJ (D3 with Becke–Johnson damping) dispersion [63] and Bader charge analysis was done by code from Dr Henkelman's group [64–66]. Strain analysis

was done by a self-made script using atomic simulation environment [67], which can be found in Github (https://github.com/shuangjiezhao).

Data availability statement

The data that support the findings of this study are available upon reasonable request from the authors.

Acknowledgment

We acknowledge stimulating discussions with Stephanie Reich and Sabrina Jürgensen. F. F., J. P., R. T. W., X. F. and T. H. acknowledge funding from the SPP 2244 (2DMP) and from the SPP 1928 (COORNETs). S. Z. acknowledges funding of the DFG priority program SPP 2244. The authors gratefully acknowledge the computing time made available to them on the high-performance computers at the NHR Centers at TU Dresden and NHR Center PC2. These are funded by the Federal Ministry of Education and Research and the state governments participating on the basis of the resolutions of the GWK for the national high-performance computing at universities (www.nhr-verein.de/unsere-partner). K.W. and T.T. acknowledge support from the JSPS KAKENHI (Grant Numbers 20H00354, 21H05233 and 23H02052) and World Premier International Research Center Initiative (WPI), MEXT, Japan.

ORCID iDs

Francesca Falorsi https://orcid.org/0009-0007-3319-7240
Christian Eckel https://orcid.org/0000-0001-7888-2574
Marcel Reutzel https://orcid.org/0000-0002-1085-2931
Kenji Watanabe https://orcid.org/0000-0003-3701-8119
Thomas Heine https://orcid.org/0000-0003-2379-6251
R Thomas Weitz https://orcid.org/0000-0001-5404-7355

References

[1] Novoselov K S, Geim A K, Morozov S V, Jiang D, Katsnelson M I, Grigorieva I V, Dubonos S V and Firsov A A 2005 Two-dimensional gas of massless Dirac fermions in graphene *Nature* **438** 197–200
[2] Novoselov K S, Geim A K, Morozov S V, Jiang D, Zhang Y, Dubonos S V, Grigorieva I V and Firsov A A 2004 Electric field effect in atomically thin carbon films *Science* **306** 666–9
[3] Novoselov K S, Mishchenko A, Carvalho A and Castro Neto A H 2016 2D materials and van der Waals heterostructures *Science* **353** aac9439
[4] Zhang Y, Tang T-T, Girit C, Hao Z, Martin M C, Zettl A, Crommie M F, Shen Y R and Wang F 2009 Direct observation of a widely tunable bandgap in bilayer graphene *Nature* **459** 820–3
[5] Mak K F, Lee C, Hone J, Shan J and Heinz T F 2010 Atomically thin MoS: a new direct-gap semiconductor *Phys. Rev. Lett.* **105** 136805
[6] Splendiani A, Sun L, Zhang Y, Li T, Kim J, Chim C-Y, Galli G and Wang F 2010 Emerging photoluminescence in monolayer MoS_2 *Nano Lett.* **10** 1271–5
[7] Kuc A, Zibouche N and Heine T 2011 Influence of quantum confinement on the electronic structure of the transition metal sulfide TS_2 *Phys. Rev.* B **83** 245213
[8] Miró P, Ghorbani-Asl M and Heine T 2014 Two dimensional materials beyond MoS_2: noble-transition-metal dichalcogenides *Angew. Chem., Int. Ed.* **53** 3015–8
[9] Miró P, Ghorbani-Asl M and Heine T 2013 Spontaneous ripple formation in MoS(2) monolayers: electronic structure and transport effects *Adv. Mater.* **25** 5473–5
[10] Feng X and Schlüter A D 2018 Towards macroscopic crystalline 2D polymers *Angew. Chem., Int. Ed.* **57** 13748–63
[11] Servalli M and Schlüter A D 2017 Synthetic two-dimensional polymers *Annu. Rev. Mater. Res.* **47** 361–89
[12] Liu K *et al* 2019 On-water surface synthesis of crystalline, few-layer two-dimensional polymers assisted by surfactant monolayers *Nat. Chem.* **11** 994–1000
[13] Liu K *et al* 2021 A two-dimensional polyimide-graphene heterostructure with ultra-fast interlayer charge transfer *Angew. Chem., Int. Ed.* **60** 13859–64
[14] Ding S-Y and Wang W 2013 Covalent organic frameworks (COFs): from design to applications *Chem. Soc. Rev.* **42** 548–68
[15] Colson J W and Dichtel W R 2013 Rationally synthesized two-dimensional polymers *Nat. Chem.* **5** 453–65
[16] Thomas S, Li H, Zhong C, Matsumoto M, Dichtel W R and Bredas J-L 2019 Electronic structure of two-dimensional π-conjugated covalent organic frameworks *Chem. Mater.* **31** 3051–65
[17] Crasto de Lima F, Ferreira G J and Miwa R H 2019 Topological flat band, Dirac fermions and quantum spin Hall phase in 2D archimedean lattices *Phys. Chem. Chem. Phys.* **21** 22344–50
[18] Löffler D *et al* 2010 Growth and structure of crystalline silica sheet on Ru(0001) *Phys. Rev. Lett.* **105** 146104
[19] Winterer F, Seiler A M, Ghazaryan A, Geisenhof F R, Watanabe K, Taniguchi T, Serbyn M and Weitz R T 2022 Spontaneous gully-polarized quantum hall states in ABA trilayer graphene *Nano Lett.* **22** 3317–22
[20] Keilmann F and Hillenbrand R 2004 Near-field microscopy by elastic light scattering from a tip Phil. Trans. R. *Soc.* A **362** 787–805
[21] Woessner A *et al* 2015 Highly confined low-loss plasmons in graphene-boron nitride heterostructures *Nat. Mater.* **14** 421–5
[22] Falkovsky L A 2008 Optical properties of graphene *J. Phys.: Conf. Ser.* **129** 12004
[23] Ni G X *et al* 2018 Fundamental limits to graphene plasmonics *Nature* **557** 530–3
[24] Basov D N, Fogler M M and García de Abajo F J 2016 Polaritons in van der Waals materials *Science* **354** aag1992
[25] Fei Z *et al* 2012 Gate-tuning of graphene plasmons revealed by infrared nano-imaging *Nature* **487** 82–85
[26] Chen J *et al* 2012 Optical nano-imaging of gate-tunable graphene plasmons *Nature* **487** 77–81
[27] Otsuki J 2010 STM studies on porphyrins *Coord. Chem. Rev.* **254** 2311–41
[28] Weitz R T, Allen M T, Feldman B E, Martin J and Yacoby A 2010 Broken-symmetry states in doubly gated suspended bilayer graphene *Science* **330** 812–6
[29] Geisenhof F R, Winterer F, Seiler A M, Lenz J, Xu T, Zhang F and Weitz R T 2021 Quantum anomalous Hall octet driven by orbital magnetism in bilayer graphene *Nature* **598** 53–58
[30] Nam Y, Ki D-K, Soler-Delgado D and Morpurgo A F 2017 Electron–hole collision limited transport in charge-neutral bilayer graphene *Nat. Phys.* **13** 1207–14

[31] Cai Y, Zhang G and Zhang Y-W 2014 Layer-dependent band alignment and work function of few-layer phosphorene *Sci. Rep.* **4** 6677
[32] Choi S, Shaolin Z and Yang W 2014 Layer-number-dependent work function of MoS_2 nanoflakes *J. Korean Phys. Soc.* **64** 1550–5
[33] Rut'kov E V, Afanas'eva E Y and Gall N R 2020 Graphene and graphite work function depending on layer number on Re *Diam. Relat. Mater.* **101** 107576
[34] Tamulewicz M, Kutrowska-Girzycka J, Gajewski K, Serafińczuk J, Sierakowski A, Jadczak J, Bryja L and Gotszalk T P 2019 Layer number dependence of the work function and optical properties of single and few layers MoS_2: effect of substrate *Nanotechnology* **30** 245708
[35] Kuhl N *et al* 2023 Utilizing biocatalysis and a sulfolane-mediated reductive acetal opening to access nemtabrutinib from cyrene *Green Chem.* **25** 606–13
[36] Ye T, Ye S, Chen D, Chen Q, Qiu B and Chen X 2012 Spectroscopic characterization of tetracationic porphyrins and their noncovalent functionalization with graphene, *Spectrochim. Acta A* **86** 467–71
[37] Lien D-H *et al* 2015 Engineering light outcoupling in 2D materials *Nano Lett.* **15** 1356–61
[38] Sleziona S, Rauls S, Heckhoff T, Christen L, Pollmann E, Madauß L, Franzka S, Lorke A, Wende H and Schleberger M 2021 Towards field-effect controlled graphene-enhanced Raman spectroscopy of cobalt octaethylporphyrin molecules *Nanotechnology* **32** 205702
[39] Ling X, Xie L, Fang Y, Xu H, Zhang H, Kong J, Dresselhaus M S, Zhang J and Liu Z 2010 Can graphene be used as a substrate for Raman enhancement? *Nano Lett.* **10** 553–61
[40] Yoon D, Moon H, Son Y-W, Choi J S, Park B H, Cha Y H, Kim Y D and Cheong H 2009 Interference effect on Raman spectrum of graphene on SiO_2/Si *Phys. Rev.* B **80** 125422
[41] Wang Y Y, Ni Z H, Shen Z X, Wang H M and Wu Y H 2008 Interference enhancement of Raman signal of graphene *Appl. Phys. Lett.* **92** 043121
[42] Malard L M, Pimenta M A, Dresselhaus G and Dresselhaus M S 2009 Raman spectroscopy in graphene *Phys. Rep.* **473** 51–87
[43] Ferrari A C and Basko D M 2013 Raman spectroscopy as a versatile tool for studying the properties of graphene *Nat. Nanotechnol.* **8** 235–46
[44] Das A *et al* 2008 Monitoring dopants by Raman scattering in an electrochemically top-gated graphene transistor *Nat. Nanotechnol.* **3** 210–5
[45] Mueller N S *et al* 2018 Evaluating arbitrary strain configurations and doping in graphene with Raman spectroscopy *2D Mater.* **5** 15016
[46] Lee J E, Ahn G, Shim J, Lee Y S and Ryu S 2012 Optical separation of mechanical strain from charge doping in graphene *Nat. Commun.* **3** 1024
[47] Keunecke M *et al* 2020 Time-resolved momentum microscopy with a 1 MHz high-harmonic extreme ultraviolet beamline *Rev. Sci. Instrum.* **91** 63905
[48] Schmitt D *et al* 2022 Formation of moiré interlayer excitons in space and time *Nature* **608** 499–503
[49] Lenz J, Statz M, Watanabe K, Taniguchi T, Ortmann F and Weitz R T 2023 Charge transport in single polymer fiber transistors in the sub-100 nm regime: temperature dependence and Coulomb blockade *J. Phys. Mater.* **6** 15001
[50] Eckel C, Lenz J, Melianas A, Salleo A and Weitz R T 2022 Nanoscopic electrolyte-gated vertical organic transistors with low operation voltage and five orders of magnitude switching range for neuromorphic systems *Nano Lett.* **22** 973–8
[51] Cooper D R *et al* 2012 Experimental review of graphene *ISRN Condens. Matter Phys.* **2012** 1–56
[52] Dutta Chowdhury D, van den Bosch F C, van Dokkum P, Robles V H, Schive H-Y and Chiueh T 2023 On the dynamical heating of dwarf galaxies in a fuzzy dark matter halo *ApJ* **949** 68
[53] Elstner M, Porezag D, Jungnickel G, Elsner J, Haugk M, Frauenheim T, Suhai S and Seifert G 1998 Self-consistent-charge density-functional tight-binding method for simulations of complex materials properties *Phys. Rev.* B **58** 7260–8
[54] Porezag D, Frauenheim T, Köhler T, Seifert G and Kaschner R 1995 Construction of tight-binding-like potentials on the basis of density-functional theory: application to carbon *Phys. Rev.* B **51** 12947–57
[55] Hourahine B *et al* 2020 DFTB+, a software package for efficient approximate density functional theory based atomistic simulations *J. Chem. Phys.* **152** 124101
[56] Frenzel J, Semi-relativistic, self-consistent charge Slater-Koster tables for density-functional based tight-binding (DFTB) for materials science simulations
[57] Blum V, Gehrke R, Hanke F, Havu P, Havu V, Ren X, Reuter K and Scheffler M 2009 *Ab initio* molecular simulations with numeric atom-centered orbitals *Comput. Phys. Commun.* **180** 2175–96
[58] Perdew J P, Burke K and Ernzerhof M 1996 Generalized gradient approximation made simple *Phys. Rev. Lett.* **77** 3865–8
[59] Hermann J and Tkatchenko A 2020 Density functional model for van der Waals interactions: unifying many-body atomic approaches with nonlocal functionals *Phys. Rev. Lett.* **124** 146401
[60] Kresse G and Furthmüller J 1996 Efficiency of *ab-initio* total energy calculations for metals and semiconductors using a plane-wave basis set *Comput. Mater. Sci.* **6** 15–50
[61] Kresse G and Furthmüller J 1996 Efficient iterative schemes for ab initio total-energy calculations using a plane-wave basis set *Phys. Rev.* B **54** 11169–86
[62] Kresse G and Joubert D 1999 From ultrasoft pseudopotentials to the projector augmented-wave method *Phys. Rev.* B **59** 1758–75
[63] Grimme S, Ehrlich S and Goerigk L 2011 Effect of the damping function in dispersion corrected density functional theory *J. Comput. Chem.* **32** 1456–65
[64] Henkelman G, Arnaldsson A and Jónsson H 2006 A fast and robust algorithm for Bader decomposition of charge density *Comput. Mater. Sci.* **36** 354–60
[65] Sanville E, Kenny S D, Smith R and Henkelman G 2007 Improved grid-based algorithm for Bader charge allocation *J. Comput. Chem.* **28** 899–908
[66] Tang W, Sanville E and Henkelman G 2009 A grid-based Bader analysis algorithm without lattice bias *J. Phys.: Condens. Matter* **21** 84204
[67] Hjorth Larsen A *et al* 2017 The atomic simulation environment-a python library for working with atoms *J. Condens. Matter Phys.* **29** 273002